Processing-structure-microscale properties of silicon nitride

Tatsuki Ohji [a,b,*], Junichi Tatami [a]

[a] *Yokohama National University, 79-5 Tokiwadai, Hodogayaku, Yokohama, Kanagawa, 240-8501, Japan*
[b] *National Institute of Advanced Industrial Science and Technology (AIST), Sakurazaka 4-205, Moriyama-ku, Nagoya, Aichi, 463-8560, Japan*

ARTICLE INFO

ABSTRACT

This paper presents an overview of recent works on microscale mechanical and other properties of silicon nitride (Si_3N_4) determined by microcantilever bending tests and their relationships with the processing and microstructures. We first focus on deformation behaviors and fracture strength of Si_3N_4 single crystals. β-Si_3N_4 single crystals are plastically deformed at room temperature under high bending stress, and the yield stress depends on the crystal orientation. The critical resolved share stress of the primary slip system is determined to be below 1.5 GPa from the yield stress. Next, we address microscale mechanical properties of Si_3N_4 polycrystalline ceramics. Emphasis is placed on their grain-boundary strength or toughness in conjunction with intergranular glassy film (IGF) which is determined by processing parameters such as sintering additives. Assessment is made on two cases of fractures at the IGF-grain interface and that within the IGF, and in each of the cases, effects of rare earth oxide additives are discussed. In Si_3N_4 ceramics doped with Al_2O_3, β-SiAlON layer forming on β-Si_3N_4 grains enhances the microscale grain-boundary strength. Finally, we shed light on microscale property-degradation behaviors of Si_3N_4 ceramics, including the deterioration due to the contact with molten Al and the corrosion in sulfuric acid solution. The variation of the microscale properties appears in very short periods compared to the macroscale approaches, demonstrating the advantage in terms of rapid assessment of time-dependent degradation behaviors.

1. Introduction

Thanks to their excellent material properties, such as high strength, high fracture toughness, low density, good heat and corrosion resistances, high thermal conductivity, and high electrical insulation, silicon nitride (Si_3N_4) ceramics have attracted a lot of attention for various engineering applications, including tribological parts, high-temperature components, metal-working tools, orthopedic implants, heat-dissipating substrates, and electronics manufacturing tools [1–13]. In the recent years, however, many of the Si_3N_4 parts used in advanced applications are becoming small and thinner. For example, Si_3N_4 ceramics have been applied to heat-dissipating substrates of power devices [10], and their thickness is now reduced to be less than a few 100 μm for improving their heat dissipation ability. Si_3N_4 thin films are being used for permeation barrier, encapsulation and passivation in various state-of-the-art devices such as microelectronics fabrication (for protection against moisture and corrosive ions), silicon solar cells (for antireflection and passivation), and microelectrode arrays (MEAs, for protection against a harsh physiological environments) [11–13]. It is

critically important to correctly evaluate and understand the mechanical behaviors of such minute parts of Si_3N_4 ceramics.

The microscale mechanical properties of ceramic single crystals and polycrystals have been investigated by several techniques. One of the most frequently used methods is nanoindentation testing, which has been recognized as a powerful tool for measuring nano- and micro-scale mechanical properties including elastic modulus, hardness, fracture toughness, creep and yield stress. This is also ideal for testing thin film and surface mechanical properties. Another common method is micro-pillar compression testing, which is a novel method for investigating the mechanical properties of materials at small length scales, including critical resolved shear stress (CRSS), elastic modulus, fracture toughness, and deformation mechanisms. However, when materials are used for structural applications, their fractures generally occur not in compression but in tension, and either nanoindentation or micropillar compression gives little information on the mechanical behaviors related to the tensile fracture. The elucidation on the microscale fracture behaviors in tension is essentially required.

The microcantilever bending test is a powerful technique that can

measure mechanical properties at a microscale with the upper part of the specimen in tension [14–32]. A load is applied at the tip of a microcantilever beam specimen to generate the bending stress on the top surface of the specimen. This method has been employed for investigating microscale mechanical performance of various ceramic materials including zirconia [14,18,29], silicon nitride [15,17,25,27,31], alumina and alumina-based ceramics [16,19], silicon carbide [20], silicon [21–23], high-entropy carbide [24], tungsten carbide [26], hydroxyapatite [27], zirconium boride [30], and glass [32]. The advantage of this approach is clarification of the whole deformation and fracture process until the final failure. This technique is also effective for evaluating microscopically the time-dependent degradation behaviors such as corrosion in combination with the mechanical properties, enabling their rapid assessment, because even if a corroded surface layer is so thin, a microcantilever beam containing the layer can reflect its change clearly.

This paper intends to present an overview of recent works on microscale properties of Si_3N_4 determined by the microcantilever bending tests and their relationships with the processing and microstructures. Following a general description on microcantilever bending tests for ceramics, we will focus on deformation behaviors and fracture strength of Si_3N_4 single crystals. The β-Si_3N_4 single crystals are plastically deformed at room temperature under high bending stress, and the yield stress depended on the crystal orientation. Next, we will address microscale mechanical properties of Si_3N_4 polycrystalline ceramics. Emphasis will be placed on their grain-boundary strength or toughness in conjunction with intergranular glassy film (IGF) which is determined by processing parameters such as sintering additives. Finally, we will shed light on microscale property-degradation behaviors of Si_3N_4 ceramics in molten aluminum and sulfuric acid solution, showing that the variation of the microscale properties appears in very short periods compared to the macroscale approaches.

2. Microcantilever bending tests

This section describes general experimental procedures for microcantilever bending tests frequently used for ceramic and glass materials. Microcantilever beam specimens are prepared from the sample materials generally using a focused ion beam (FIB) technique. A schematic illustration of a specimen we use for measurements of bending strength and Young's modulus is shown in Fig. 1 (a), with an example of a single crystal specimen (Fig. 1 (b)). The section profile is mostly selected to be pentagonal or triangular, so that the bottom part is machinable from above by a FIB processing. The pentagonal shape is more preferable because of the larger second moment area and the smaller influence of the specimen asymmetry. The width, thickness, and length of the microcantilever specimens reported so far range in 0.5–7 μm, 1–7 μm, and 5–25 μm, respectively [14–32]. In this review article, they are 1~2 μm, 2–3 μm, and 12–15 μm, respectively, unless otherwise noted.

Microcantilever bending tests are carried out by applying a load at a point on the center line near the free end of a specimen. The measured displacement of the indenter generated during the bending test includes both the depth of the indent itself and the deflection of the specimen at the loading point. Therefore, Yamauchi et al. [23], Tanabe et al. [27], and Muramoto et al. [29] obtained a true displacement at the loading point by subtracting an indentation depth measured when the indentation is made on a flat surface of the same sample material using the same indenter with the same loads.

When the displacement is small, the bending stress, σ, the strain, ε, and the Young's modulus, E, of the specimen are obtained from the load and displacement using the following equations based on the elastic beam theory:

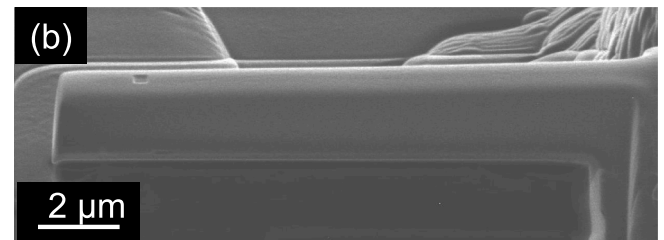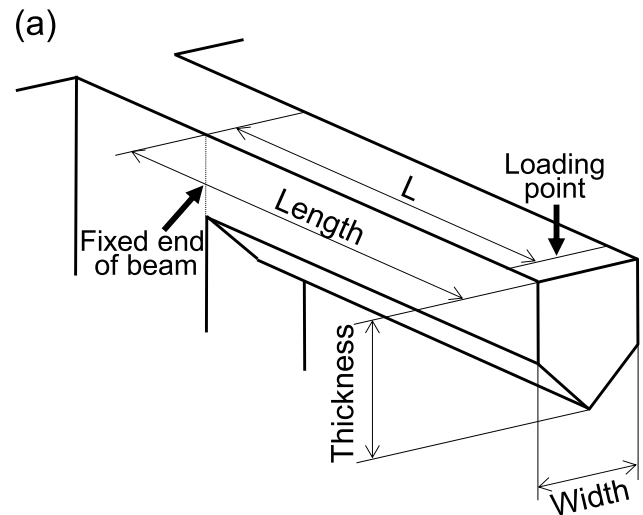$$\sigma = \frac{PL\delta a}{I} \tag{1}$$

Fig. 1. (a) Schematic illustration of a microcantilever beam specimen for measurements of bending strength and Young's modulus. (b) Example of a specimen (β-Si_3N_4 single crystal) [27]. The width, thickness, and length were approximately 1.5, 2.5, and 12 μm, respectively.

$$\varepsilon = \frac{3d\delta a}{L^2} \tag{2}$$

$$E = \frac{PL^3}{3dI} \tag{3}$$

where *P* is the applied load, *L* is the load point distance (See Fig. 1(a)), δa is the distance between the top surface and the neutral plane, *I* is the second moment of area calculated for the cross section, and *d* is the displacement at the loading point. The sectional shape and sizes of each specimen should be determined precisely for calculation of *I*. A trapezoidal approximation (see "Supplementary Material (1)") is one of the most frequently employed methods for this determination. The bending strength (or fracture strength) and yield stress were determined from the maximum load and the load at the proportional limit of the curve, respectively, using Eq. (1). It should be noted, however, that the stress calculated assuming the elastic beam theory (Eq. (1)) is not entirely identical with that of a numerical analysis. For example, Muramoto et al. [29] conducted finite element analyses (FEA) for the microcantilever beam specimen shown in Fig. 1 (a) and revealed that that both the maximum normal stress and the loading-point-displacement linearly increased with increasing the applied load; however, the state of the stress distribution was not exactly homogeneous, and the maximum normal stress, which arose not precisely at the fixed end but slightly away (~0.5 μm for 10 μm L) to the free end, was ~6 % lower than that of the beam theory.

Fig. 2 (a) shows a schematic illustration of a microcantilever beam specimen used for the fracture toughness measurements in this review article, with an example of a notch introduced into Si_3N_4 ceramics (Fig. 2 (b)). The shape and sizes of the specimen are basically the same as those of the bending strength measurements, and a sharp notch with a
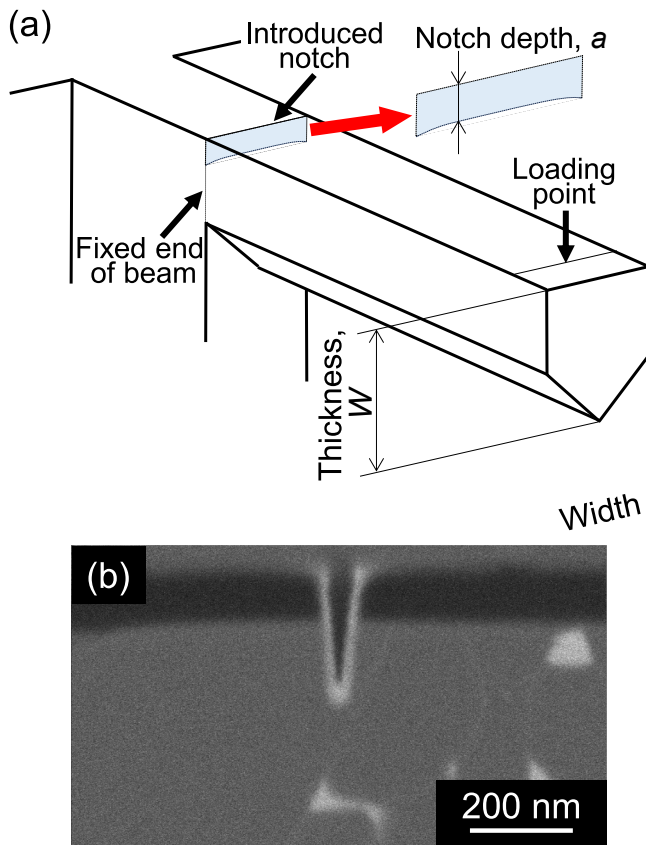
Fig. 2. (a) Schematic illustration of a microcantilever beam specimen for measurements of fracture toughness. The notch depth is not exactly uniform but tends to be larger at both the side surfaces than at the central area. (b) Example of a notch introduced into Si_3N_4 ceramics [17].

depth of approximately 200 nm and a tip radius less than 15 nm was introduced by FIB machining at the fixed end of the beam. The notch depth and tip radius as well as the specimen shape and sizes were measured by SEM observation. Fracture tests similar to the bending strength measurements were carried out to obtain fracture loads. In principle, the fracture toughness, K_{IC}, is given by $K_{IC} = \sigma_f \sqrt{\pi a}\, F(a/W)$, where σ_f is the fracture stress, a is the notch depth, F is the shape factor, and W is the specimen thickness. However, the depth of a notch introduced by FIB machining is not exactly uniform but tends to be larger at both the side surfaces than at the central area (Fig. 2 (a)). Therefore, the fracture toughness was determined using a finite element method (FEM) analysis based on the accurate geometry measurement of the specimen and notch and the fracture load (see "Supplementary Material (2)").

3. Microscale mechanical properties Si_3N_4 single crystals

Many of the state-of-the art devices tend to be smaller and thinner in recent years. In such cases, the single-crystal grains themselves play a significant role in determining the material properties. For ensuring their structural reliability it is critically important to correctly evaluate and understand the deformation behaviors and mechanical properties of Si_3N_4 single crystals. Csanádi et al. [33] reported that β-Si_3N_4 single crystal undergo plastic deformation when the compressive stress exceeds the yield stress due to the generation and movement of dislocations in the primary slip system $\{10\bar{1}0\}<0001>$ by means of micropillar compression tests; the CRSS in this system was estimated to be 1.64 GPa.

Using the microcantilever beam specimens, Tanabe et al. [27] evaluated the deformation behaviors and fracture strength of β-Si_3N_4 single crystals having different angles of tensile-stress application from

the c-axis and elucidated their dependence on the crystal orientations. They first prepared Si_3N_4 polycrystals by using α-Si_3N_4 powder with sintering additives of 3 wt% Y_2O_3 and 7 wt% MgO (Si_3N_4:Y_2O_3:MgO = 90:3:7, the same applies hereafter) and sintering at 1950°C for 6 h in 0.9 MPa N_2 and obtained sintered bodies of relative densities>98 % having a microstructure of elongated β-Si_3N_4 grains. The crystal orientation mapping was performed by electron backscattering diffraction (EBSD) analysis, and large grains were selected so that the area where a tensile stress arises is fully covered by a single crystal with identifying the crystal orientation. The specimens were cut prepared by varying the angle, θ, between the tensile stress direction (specimen's longitudinal direction) and the grain's c-axis (see the insert of Fig. 3).

Fig. 3 shows examples of the stress–strain curves obtained for the specimens of θ = 3° and 22.8°. After the stress increases linearly with the strain in the low-stress range, the nonlinear or plastic deformation appears at a specific stress, or a yield stress. The obtained relationship between the angle θ and the yield stress is shown in Fig. 4, together with the CRSS and bending strength which are to be discussed later. The yield stress tends to increase as the angle θ approaches 0. The transmission electron microscopy (TEM) study for the deformed specimen of the angle θ of 23.8° (observed in the $[11\bar{2}0]$ direction) revealed the broad strain contrasts in the region where the highest bending stress arose, as shown in Fig. 5 (a). These contrasts have been typically observed in β-Si_3N_4 single crystals plastically deformed at high temperatures in previous studies. Fig. 5 (b) shows a high-resolution TEM image of the region where such strain contrasts appeared. Strong lattice disorder is observed in the [0001] direction, which agrees with the observation that the primary slip system of β-Si_3N_4 single crystals is the slip plane $\{10\bar{1}0\}$ with the slip direction $<0001>$, as reported by many researchers [34–36]. The CRSS with the primary slip system was calculated for the specimens of different angle θ using the yield stress as the tensile stress when the slip occurred, as shown in Fig. 4. It is almost constant regardless of θ, and the average value is 1.34 ± 0.55 GPa, which agrees well with the above-stated CRSS value, 0.1–1.6 GPa, reported by Csanádi et al. [33].

The obtained bending strength of β-Si_3N_4 single crystals is shown in Fig. 4. The strength of the specimens whose tensile direction is parallel to the c-axis, is very high, approximately 20 GPa. The average bending
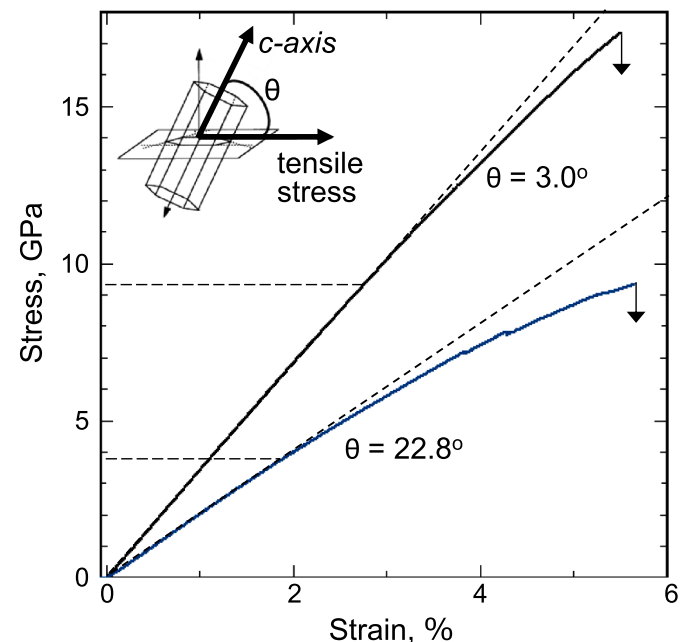

Fig. 3. Stress–strain curves for the microcantilever beam specimens of β-Si_3N_4 single crystals with θ = 3.0° and 22.8°. The horizontal dotted line indicate the proportional limit or the yield stresses [27].

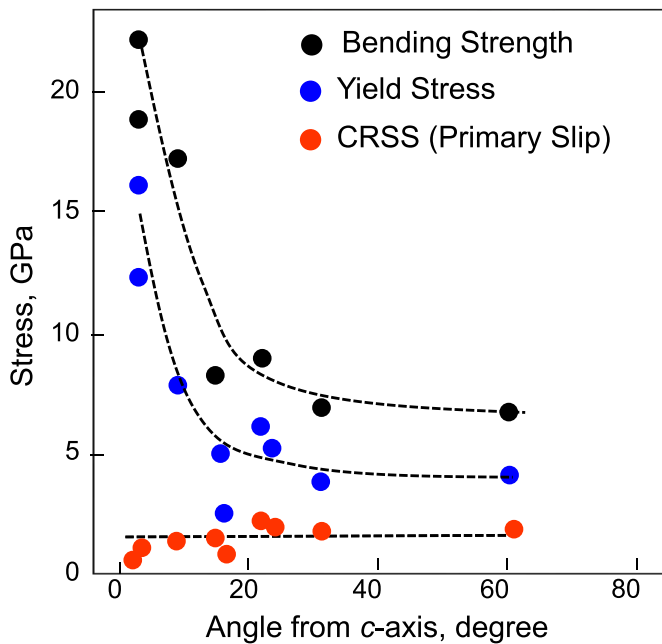**Fig. 4.** Yield stress, CRSS (Critical resolved shear stress), and bending strength of β-Si₃N₄ single crystals as a function of θ [27].
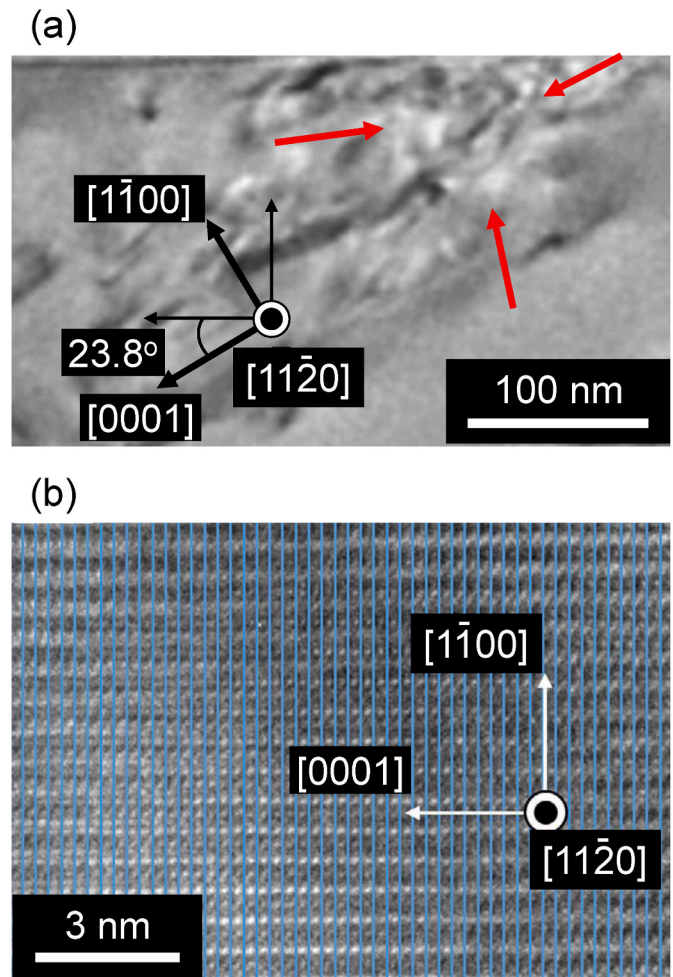

Fig. 5. (a) TEM image of broad strain contrasts in the region where the highest bending stress arose in the deformed specimen of the angle θ of 23.8° (observed in the [11 $\overline{2}$ 0] direction). The concentrated area of lattice disorder with a size of about 100 nm is indicated by red arrows. (b) High resolution TEM image of such a strain contrast [27]. (For interpretation of the references to colour in this figure legend, the reader is referred to the Web version of this article.)

strength was 12.4 ± 5.4 GPa, which agreed well with the bending strength of β-Si₃N₄ grains, 10.5 ± 0.8 GPa, measured by Csanádi et al. [25] using microcantilever bending tests, though the crystal orientation was not identified in their study. Based on linear fracture mechanics, the Grifith crack length was estimated to be about 90 nm for the specimen of 23.8° θ from the strength, 7.5 GPa, and the fracture toughness, 2.77 MPa m$^{1/2}$ [15]. Fig. 5 (a) shows a concentrated area of lattice disorder with a size of about 100 nm (indicated by red arrows), which is in good agreement with the above estimated crack length. Dislocation pileups result in stress concentration and/or crack formation, which possibly resulting in a fracture origin of a material [37]. Particularly the dislocation pileups moving on a slip plane can promote mode II crack formation and control the strength of β-Si₃N₄ single crystals. It is also generally known that one typical source of cracks is the interaction of different slips, causing dislocation pileups and cleavage cracks generated at the intersections of two different slip planes. They may act as a fracture origin controlling the strength. The dislocation pileups are thought to be more intense with lowering the yield stress. As a result, the fracture strength and the yield stress have the similar dependency on the angle θ.

4. Microscale mechanical properties Si₃N₄ polycrystals

4.1. Grains, grain boundaries, and polycrystals

The previous section described that the CRSS with the primary slip system is 1.34 ± 0.55 GPa, indicating that Si₃N₄ single crystals can deform in a specific direction at this shear stress or higher. However, the von Mises criterion [38] requires that five independent slip systems must operate for polycrystals to deform uniformly without failure at the grain boundaries (It should be noted that a recent review on this subject indicated that three linearly independent slip systems are essentially sufficient for compatible deformation [39]). Because Si₃N₄ polycrystals do not satisfy this criterion (even three independent slip systems), they do not deform plastically at least at room temperature, and brittle fractures are observed in their load-displacement diagrams of bending tests.

Si₃N₄ is a typical difficult-to-sinter material and therefore its polycrystals are usually produced by using sintering additives such as oxide

ceramics. The additives form liquid phase at elevated temperatures, which enhances the solution-reprecipitation processes leading to the densification during sintering. Upon cooling, the liquid remains as grain-boundary glassy films (typically 1 nm thick) and secondary crystal or amorphous phases at multigrain junctions. These grain boundaries play a critical role in determining mechanical properties of Si₃N₄ polycrystals.

Tatami et al. [15] investigated fracture toughness of Si₃N₄ polycrystalline ceramics using single-edge notched microcantilever beam specimens(Fig. 2 (b)), with three measurement targets including grains, grain boundaries, and polycrystals (comprising both). The materials were sintered using α-Si₃N₄ powder with 5 wt% Y₂O₃ and 3 wt% Al₂O₃ for 2 h in 0.9 MPa N₂; the sintering temperature was 1800 °C for polycrystals and 1900 °C for grains and grain boundaries, since the latter needed larger grains. Fig. 6 shows SEM photographs of microstructures of the prepared Si₃N₄ polycrystalline ceramics, together with those doped with La₂O₃- and Lu₂O₃-based additives which are to be discussed later. Dense sintered bodies having microstructures of large, elongated grains embedded in fine matrix ones are obtained.

Table 1 shows the measured fracture toughness values for grains, grain boundaries, and polycrystals. The value of grains is higher than that of grain boundaries, and the toughness of polycrystals is an intermediate between them. Fig. 7 shows their plots together with an *R* curve
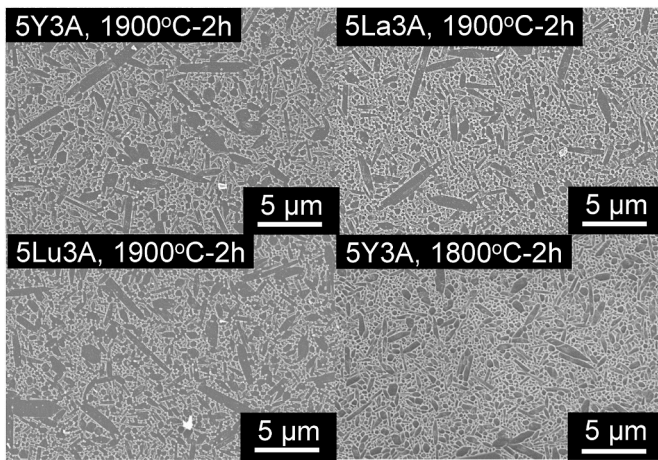
Fig. 6. SEM photographs of microstructures of Si₃N₄ polycrystalline ceramics. 5Y3A,5La3A, and 5Lu3A indicate the sintering additives of 5 wt% Y_2O_3-3 wt% Al_2O_3, 5 wt% La_2O_3-3 wt% Al_2O_3, and 5 wt% Lu_2O_3-3 wt% Al_2O_3, respectively [15]..

Table 1
Fracture toughness of grain boundaries, grains, and polycrystals of Si₃N₄ ceramics measured using single-edge notched microcantilever beam specimens. Differential binding energies (Si reference), DBE, and cationic field strengths, CFS, of RE ions of sintering additives are also shown [15].

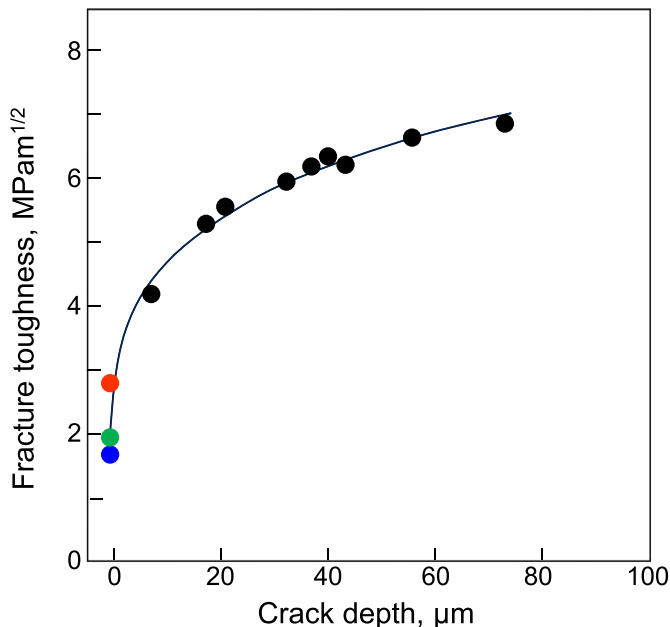|	Sintering additives	Fracture toughness, MPa.m$^{1/2}$	DBE of RE, eV	CFS of RE, Å^{-2}
Grain boundary	La_2O_3–Al_2O_3	1.63 ± 0.60	-0.98	2.18
	Y_2O_3–Al_2O_3	1.73 ± 0.52	~0	2.77
	Lu_2O_3–Al_2O_3	2.28 ± 0.37	2.50	3.19
Grain	Y_2O_3–Al_2O_3	2.77 ± 0.54	–	–
Polycrystal	Y_2O_3–Al_2O_3	1.92 ± 0.37	–	–

Fig. 7. Fracture toughness values for grains (●), grain boundaries (●), and polycrystals (●) in comparison with toughness (●) and an R curve for Si₃N₄ ceramics (doped with Y_2O_3) measured by a surface-crack in flexure (SCF) method [15,40].

for Si₃N₄ ceramics (doped with Y_2O_3) measured by a surface-crack-in flexure (SCF) method [40]. The value at the zero crack-depth extrapolated from the *R* curve agrees with that of polycrystals, because the toughness measured by single-edge notched microcantilever beam specimens is free of crack-shielding toughening effects including grain bridging and pull-out.

4.2. Rare earth oxide additives and grain boundary properties

As above stated, glassy films remain at grain boundaries of Si₃N₄ ceramics as IGF, and the IGF thickness ranges in 0.5 nm–1.5 nm, depending on the film chemistry (It has been also known that this result, the independence of the IGF thickness from grain orientation, is unexpected and not predicted by theory) [41]. It can be considered that, if the fracture occurs at the grain boundaries, it originates either at the interface between the grains and the IGF or within the IGF, depending on the film's composition. For example, Becher et al. [42] reported that the crack propagation path observed in grain-boundary fractures of Si₃N₄ ceramics doped with Y_2O_3 and Al_2O_3 is shifted from solely that along the IGF-grain interface to mixture of those along the interface and within the IGF, when increasing the Y_2O_3 to Al_2O_3 ratio.

Tatami et al. [15] also prepared Si₃N₄ ceramics doped with 5 wt% La_2O_3 and 3 wt% Al_2O_3 and those with 5 wt% Lu_2O_3 and 3 wt% Al_2O_3 via sintering at 1900 °C for 2 h in 0.9 MPa N_2 (Fig. 6) and investigated fracture toughness for their grain boundaries using the same microcantilever beam specimens as above. The results are shown also in Table 1. It should be noted that the value decreases with increasing the ionic radius (Lu < Y < La). As described in the above, this value derives either from the fracture at the IGF-grain interface or that within the IGF.

In terms of the IGF-grain interface, it is known that its strength is substantially affected by the rare earth (RE) cations which segregate to the grain surfaces in Si₃N₄ ceramics. The segregated RE cations also govern the grain growth behavior and resultantly their aspect ratios. Painter et al. [43] introduced a first-principles-based energy parameter, differential binding energy, DBE, which provides a second-difference measure of relative site stabilities of RE vs Si atoms for different O/N contents. When the DBE value of an additive cation is negative, it is more energetically favorable for the cation to segregate to the nitrogen-rich grain surfaces than Si. On the other hand, a cation with positive DBE has a greater affinity for oxygen than Si and tends to reside within the IGF. Some atomic resolution STEM studies on the segregation behavior and specific adsorption sites for RE cations confirmed this theory [44–48]. Effects of the RE intergranular adsorption on the phase transformation, microstructure evolution, and mechanical properties in Si₃N₄ ceramics were also investigated [49–52]. The DBE values (Si reference) for La, Y and Lu are shown in Table 1, indicating that the amount of the RE cations which segregate to the IGF-grain interface and replace Si ions increases in order of Lu < Y < La. Because these RE cations work as glass network modifiers rather than network formers such as Si ions [53,54], their presence weakens the IGF-grain interface. Therefore, it is reasonable that the fracture toughness values of grain boundaries increase in order of La < Y < Lu, as shown in Tables 1 and if the grain boundary facture occurs at the IGF-grain interface.

When considering the case that the grain boundaries facture from the inside of the IGF, the IGF's strength is influenced by the different additive RE cations in various factors including the elasticity, thermal expansion coefficient, film thickness, etc. One of the most influential parameters is the cationic field strength, CFS, expressed as follows:

$$CFS = \frac{Z}{r_i^2} \tag{4}$$

where Z is the valence of the RE cation and r_i its ionic radius. Table 1 shows the calculated CFS, for La, Y, and Lu [55,56]. The CFS increases in order of La < Y < Lu, which agrees with the increase of the fracture toughness of the grain boundaries.

However, a latest study on fracture strength of grain boundaries for Si_3N_4 ceramics doped with 3 wt% RE_2O_3 (RE = La, Y, or Lu) and 7 wt% MgO using microcantilever beam specimens showed a different order of strength in terms of RE from the above results on the fracture toughness, La < Y < Lu; the grain-boundary strength increased in order of Y < La < Lu [57]. It should be noted that the fracture toughness should be proportional to the bending strength because no toughening effect works in this case. This order of the grain-boundary strength, Y < La < Lu, agrees with the study by Satet et al. [49], who investigated influence of intergranular phase composition on fracture toughness of Si_3N_4 ceramics using MgO and RE_2O_3 (RE = La, Y, Lu, etc.) as sintering additives. The microstructure was tailored to have the same grain sizes and morphologies by adjusting the sintering parameters, so that the fracture toughness reflects the debonding behavior of the grain boundary. The toughness increased in order of Lu < La < Y, indicating that the grain-boundary strength decreased in Lu > La > Y. It was suggested that O anions, which reside within the IGF and do not dissolve into the β-Si_3N_4 crystal lattice because of the high cationic field strength at the small ionic radius, reduce the grain-boundary strength [57].

Csanádi et al. [25] investigated microscale fracture strength of grains and grain boundaries in polycrystalline La-doped β-Si_3N_4 ceramics using microcantilever beam specimens (pentagonal cross-sections with lengths of 11.7–23.2 μm, widths of 2.1–6.3 μm and thicknesses of 2.1–5.7 μm). The fracture behavior of SiO_2–La_2O_3 intergranular glassy phase between β-Si_3N_4 grains was also modelled by ab initio simulations, and the obtained theoretical predictions were compared with the experimental results. The measured fracture strength along the grain boundaries decreased from 2.9 GPa to 2.1 GPa with increasing the La_2O_3 content from 0.86 wt% to 4.19 wt%. The results qualitatively agreed well with the predictions by ab initio simulations, confirming that the existence of RE cations weakens the grain boundaries.

4.3. Alumina additives and grain boundary properties

It has been well known that a distinct epitaxial β-SiAlON layer readily forms on β-Si_3N_4 grains in glasses having high alumina and nitrogen contents. It can be considered that, compared to the β-Si_3N_4/ oxynitride-glass interface, the β-SiAlON/oxynitride-glass interface is more resistant to debonding or possesses a higher bonding strength, because the Al and O are distributed more gradually across the latter interface than across the former [58–60]. β-SiAlON contains Al–N, Al–O, and Si–O bonds in addition to Si–N bonds, while Si–Al–Y oxynitride glasses do Si–O, Si–N, Al–N, and Al–O, indicating that similar chemical bonds exist in the two phases. Thus, the SiAlON/glass interface has a potential to be more strongly chemically bonded than the Si_3N_4/glass interface [58].

Table 2 shows the bending for two types of Si_3N_4 ceramics determined using the same microcantilever bending test procedure. One is sintered with additives of 5 wt% Y_2O_3 and 5 wt% Al_2O_3 [17] and the other with 5 wt% Y_2O_3 and 3 wt% Al_2O_3 [31]. The preparation procedures are almost the same, resulting in nearly identical microstructures (grain sizes and morphologies). The fractographic studies revealed that the intergranular factures were predominant in both the cases, indicating the measured value is the grain boundary strength. The former strength is~1.2 GPa higher than the latter, and this discrepancy is most likely due to the difference of the ratio of the sintering additives, Y_2O_3 and Al_2O_3. It has been reported that, in Si_3N_4 ceramics doped with Y_2O_3 and Al_2O_3, even slight difference of Y:Al ratio, such as 4:2.8 vs. 5:2 in weight, substantially affects the interfacial debonding between the β-Si_3N_4 grains and the intergranular glassy phase, resulting in the different fracture toughening behaviors and *R*-curve responses [58].

It should be also noted that Al cations can act as a network former depending on the coordination number [61], while RE cations such as Y do as a network modifier as stated in the above. Therefore, the strength of the glass itself is plausibly reduced when increasing the Y:Al ratio, leading to more fragility of the inside of the IGF. As shown in the above, the grain-boundary crack propagation Si_3N_4 ceramics doped with Y_2O_3 and Al_2O_3 is shifted from solely that along the IGF-grain interface to the appearance of fractures within the IGF, when increasing the Y:Al ratio [42]. This is most likely because of the weaker IGF at higher Y:Al ratios.

5. Microscale property-degradation of Si_3N_4 polycrystals

5.1. Degradation of Si_3N_4 ceramics in contact with molten al

One of the structural advantages of Si_3N_4 ceramics is their good corrosion resistance, and therefore, this material is most often utilized as structural components in corrosive environments such as Al casting process [62]. In this application, Si_3N_4 ceramic components are soaked in molten Al at about 750°C, and their structural reliabilities are deteriorated after long-term use. This type of evaluation of the degradation behavior using actual components requires prolonged periods of time, typically several years.

Besides the reliability assurance of micro-components as described in the previous sections, another advantage of the microscale evaluation is the rapid assessment of the time-dependent degradation behaviors such as corrosion. Fujita et al. [17] studied the mechanical properties of surface layers of Si_3N_4 ceramics after contact with molten Al at 750°C for 6 h in air, using microcantilever beam specimens. The material was sintered at 1750°C for 2 h in 0.9 MPa N_2 using α-Si_3N_4 powder with additives of 5 wt% Y_2O_3 and 5 wt% Al_2O_3. The visible degradation in the mechanical properties appeared only after this short period's immersion, as shown in Table 3. All of the bending strength, fracture toughness and Young's modulus decreased after the molten Al contact. Table 3 also exhibits equivalent crack sizes obtained from the strength and toughness assuming a Griffith crack. Since they are almost the same before and after the molten Al contact (or the latter is even smaller than the former), the strength degradation can be considered due to the decrease in the toughness. The oxynitride glass existing at grain boundaries of Si_3N_4 ceramics consists mainly of SiO_2 glass network. It has been known that SiO_2 glass reacts with molten Al to produce Al_2O_3 by the following replacement reaction [63–65].

$$3SiO_2 + 4Al \rightarrow 2Al_2O_3 + 3Si \tag{5}$$
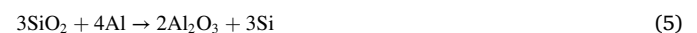
Due to the difference in volume between $3SiO_2$ and $2Al_2O_3$, this reaction results in ~27 % volume shrinkage, leading to formation of microcracks and micro-voids at the grain boundaries. Fig. 8 shows SEM images of the fractured surface morphologies of specimens. Unusual net-like morphology with traces of micro-voids was observed on the fractured grain boundary after the molten Al contact. Although microcracks are generally invisible in SEM observation, it is most plausible that the formation of micro-cracks or micro-voids) reduces the Young's modulus as well as the fracture toughness, as shown in Table 3. In addition, ion-

Table 2
Grain boundary strength determined by microcantilever bending tests for Si_3N_4 ceramics with Y_2O_3–Al_2O_3 sintering additives of different contents [17,31].

Sintering additives	Bending strength, GPa
5 wt% Y_2O_3 - 5 wt% Al_2O_3	5.89 ± 1.19 GPa
5 wt% Y_2O_3 - 3 wt% Al_2O_3	4.62 ± 0.6 GPa

Table 3
Mechanical properties of Si_3N_4 ceramics determined by microcantilever bending tests before and after contact with molten Al at 750°C for 6 h in air [17].

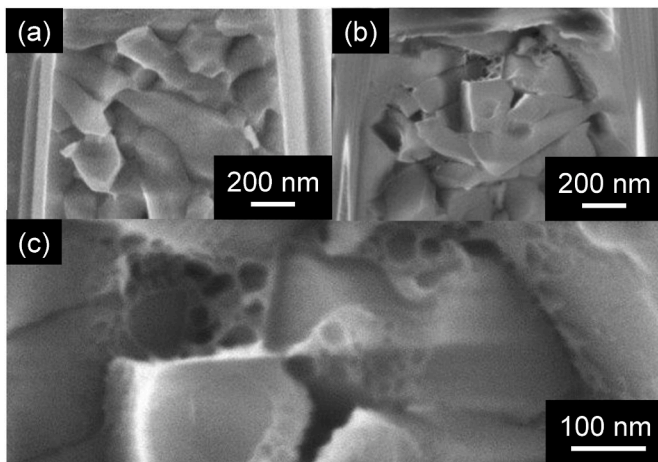|	Before	After
Bending strength, GPa	5.89 ± 1.19	3.03 ± 0.28
Fracture toughness, MPa.m$^{1/2}$	3.28 ± 0.61	1.60 ± 0.43
Young's modulus, GPa	343	212
Equivalent crack size, nm	99	89

Fig. 8. SEM images of the fractured surfaces of specimens: before (a) and after (b) contact with molten Al at 750°C for 6 h in air; (c) is the enlarged view of (b) [17].
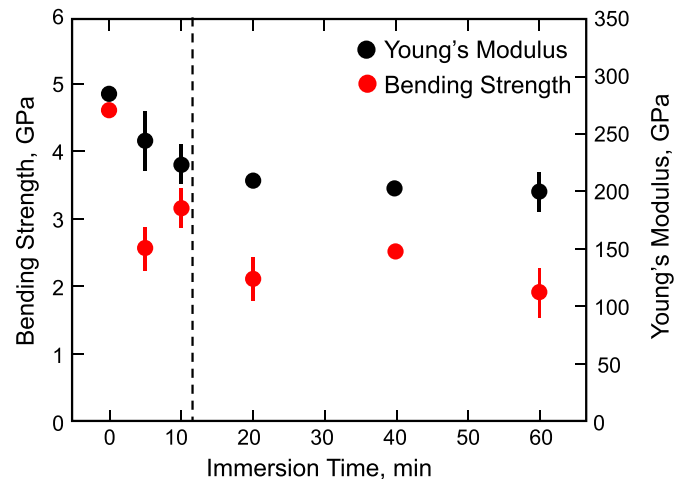

Fig. 9. Bending strength and Young's modulus determined by microcantilever bending tests as a function of immersion time. The vertical dotted line denotes that the corrosion layer thickness reaches the specimen's bottom [31].

exchange between Y and Al cations can take place in the grain boundary oxynitride glass. It has been reported that the fracture toughness of oxynitride glass containing Y and Al cations decreases with an increase in Y/Al ratio when the N and Si contents are the same [66], most likely due to the difference between the network modifier and former, as discussed in the above.

5.2. Corrosion of Si$_3$N$_4$ ceramics in sulfuric acid solution

Another example for rapid evaluation of property-degradation behavior using microcantilever beam specimens is the study on microscale mechanical properties including bending strength and Young's modulus for Si$_3$N$_4$ ceramics which was immersed in 5 wt% sulfuric acid solution at 80°C [31]. The sample was prepared by sintering at 1700°C for 2 h in 0.9 MPa N$_2$ using α-Si$_3$N$_4$ powder with additives of 5 wt% Y$_2$O$_3$ and 3 wt% Al$_2$O$_3$. The results were discussed in comparison with the macroscopic results obtained in conventional three-point bending tests with 3 mm height, 4 mm width and 30 mm span length. Fig. 9 shows the microcantilever bending strength and Young's modulus as a function of the immersion time. The top tensile surface of the microcantilever beam specimen is acid-immersed, and the vertical dotted line of Fig. 9 denotes that the estimated corrosion layer thickness reaches the specimen's bottom; in other words, the whole specimens are corroded. Both the bending strength and Young's modulus sharply drop in several minutes. The properties degradations are due to the dissolutions of Y and Al cations of grain-boundary glassy phase, followed by the hydration where the cations of large ionic radii are exchanged for the protons. After the drops at the beginning of the corrosion, both the properties show little degradation afterwards due to a relatively strong network structure remaining at the grain boundaries. The observed corrosion degradation behaviors of the mechanical properties are basically the same as those in conventional macroscopic approaches; however, the properties changes appear in very short periods of the corrosion in the microcantilever bending tests, compared with the macroscopic methods which typically need several 10 h for the similar degradation of the strength to come out.

6. Summary

This paper presented an overview of recent works on microscale mechanical and other properties of Si$_3$N$_4$ determined by the microcantilever bending tests and their relationships with the processing and microstructures. After the general description on microcantilever bending tests, we focused on the deformation behaviors and fracture strength of Si$_3$N$_4$ single crystals. The β-Si$_3$N$_4$ single crystals were

plastically deformed at room temperature under high bending stress, and the yield stress depended on the crystal orientation. The CRSS of the primary slip system determined from the yield stress was below 1.5 GPa. Next, we addressed the microscale fracture strength of Si$_3$N$_4$ polycrystalline ceramics. The particular emphasis was placed on their grain-boundary strength or toughness in conjunction with the IGF which was determined by processing parameters such as sintering additives. The assessment was made on the two cases of the fracture at the IGF-grain interface and that within the IGF, and in each of the cases, the effects of RE oxide additives were discussed. When Al$_2$O$_3$ was doped as a sintering additive, β-SiAlON layer forming on β-Si$_3$N$_4$ grains had a potential to be strongly chemically bonded to the IGF and affected the microscale grain-boundary strength. Finally, we shed light on microscale property-degradation behaviors of Si$_3$N$_4$ ceramics, including the deterioration due to the contact with molten Al and the corrosion in the sulfuric acid solution. The variation of the microscale properties appeared in very short periods compared to the macroscale approaches, demonstrating the advantage in terms of rapid assessment of time-dependent degradation behaviors.

CRediT authorship contribution statement

Tatsuki Ohji: Conceptualization, Investigation, Writing – original draft. **Junichi Tatami:** Conceptualization, Funding acquisition, Investigation, Project administration, Supervision, Writing – review & editing.

Declaration of competing interest

The authors declare that they have no known competing financial interests or personal relationships that could have appeared to influence the work reported in this paper.

Acknowledgements

Appendix A. Supplementary data

Supplementary data to this article can be found online at https://doi.org/10.1016/j.ceramint.2024.04.238.

References

[1] S. Hampshire, Silicon nitride ceramics, in: T. Ohji, M. Singh (Eds.), Engineered Ceramics, John Wiley & Sons, Inc., Hoboken, 2016, pp. 77–97, https://doi.org/10.1002/9781119100430.ch5.

[2] F.L. Riley, Silicon nitride and related materials, J. Am. Ceram. Soc. 83 (2000) 245–265, https://doi.org/10.1111/j.1151-2916.2000.tb01182.x.

[3] K. Komeya, Seeds Innovation and Bearing applications of silicon nitride ceramics, Ceram. Eng. Sci. Proc. 32 (2011) 1–15, https://doi.org/10.1002/9781118095379.ch1.

[4] H. Klemm, Silicon nitride for high-temperature applications, J. Am. Ceram. Soc. 93 (2010) 1501–1522, https://doi.org/10.1111/j.1551-2916.2010.03839.x.

[5] D.-W. Tan, L.-L. Zhu, W.-X. Wei, J.-J. Yu, Y.-Z. Zhou, W.-M. Guo, H.-T. Lin, Performance improvement of Si₃N₄ ceramic cutting tools by tailoring of phase composition and microstructure, Ceram. Inter. 46 (2020) 26182–26189, https://doi.org/10.1016/j.ceramint.2020.07.116.

[6] M.C. Anderson, R. Olsen, Bone ingrowth into porous silicon nitride, J. Biomed. Mater. Res. 92A (2010) 1598–1605, https://doi.org/10.1002/jbm.a.32498.

[7] J. Olofsson, T.M. Grehk, T. Berlind, C. Persson, S. Jacobson, H. Engqvist, Evaluation of silicon nitride as a wear resistant and resorbable alternative for total hip joint replacement, Biomatter 2 (2012) 94–102, https://doi.org/10.4161/biom.20710.

[8] D.T. Spencer, J.F. Bauters, J.E. Bowers, Integrated waveguide coupled Si₃N₄ resonators in the ultrahigh-Q regime, Optica 1 (2014) 153–157, https://doi.org/10.1364/OPTICA.1.000153.

[9] T. Yahagi, D. Kawai, T. Takahashi, M. Iijima, J. Tatami, Electrical resistivity of Si₃N₄ ceramics with Yb₂O₃ additive, J. Am. Ceram. Soc. 105 (2022) 2046–2057, https://doi.org/10.1111/jace.18211.

[10] Y. Nakashima, Y. Zhou, K. Tanabe, S. Arima, K. Hirao, T. Ohji, N. Murayama, M. Fukushima, Effect of microstructures on dielectric breakdown strength of sintered reaction-bonded silicon nitride ceramics, J. Am. Ceram. Soc. 106 (2023) 1139–1148, https://doi.org/10.1111/jace.18826.

[11] A.E. Kaloyeros, F.A. Jove, J. Goff, B. Arkles, Review - silicon nitride and silicon nitride-rich thin film Technologies: Trends in Deposition techniques and related applications, ECS J. Solid State Sci. Technol. 6 (2017) 691–714, https://doi.org/10.1149/2.0011710jss.

[12] A. E. Kaloyeros, Y. Pan, J. Goff, B. Arkles, Review - Silicon Nitride and Silicon Nitride-Rich Thin Film Technologies: State-of-the-Art Processing Technologies, Properties, and Applications, ECS J. Solid State Sci. Technol. 9, 063006. https://doi.org/10.1149/2162-8777/aba447.

[13] A. Karttu K. Lahtonen, J. Heikkilä, J. Väliaho, S. Narkilahti, J. Lekkala, P. Kallio, Corrosion and protection of silicon nitride Insulators in microelectrode array applications, IEEE Sensor. J. 22 (2022) 12504–12514, https://doi.org/10.1109/JSEN.2022.3178640.

[14] E. Camposilvan, O. Torrents, M. Anglada, Small-scale mechanical behavior of zirconia, Acta Mater. 80 (2014) 239–249, https://doi.org/10.1016/j.actamat.2014.07.053.

[15] J. Tatami, M. Katayama, M. Ohnishi, T. Yahagi, T. Takahashi, T. Horiuchi, M. Yokouchi, K. Yasuda, D.K. Kim, T. Wakihara, K. Komeya, Local fracture toughness of Si₃N₄ ceramics measured using single-edge notched microcantilever beam specimens, J. Am. Ceram. Soc. 98 (2015) 965–971, https://doi.org/10.1111/jace.13391.

[16] A.D. Norton, S. Falco, N. Young, J. Severs, R.I. Todd, Microcantilever investigation of fracture toughness and subcritical crack growth on the scale of the microstructure in Al₂O₃, J. Eur. Ceram. Soc. 35 (2015) 4521–4533, https://doi.org/10.1016/j.jeurceramsoc.2015.08.023.

[17] S. Fujita, J. Tatami, T. Yahagi, T. Takahashi, M. Iijima, Degradation evaluation of Si₃N₄ ceramic surface layer in contact with molten Al using microcantilever beam specimens, J. Eur. Ceram. Soc. 37 (2017) 4351–4356, https://doi.org/10.1016/j.jeurceramsoc.2017.01.016.

[18] R. Henry, T. Blay, T. Douillard, A. Descamps-Mandine, I. Zacharie-Aubrun, J.-M. Gatt, C. Langlois, S. Meille, Local fracture toughness measurements in polycrystalline cubic zirconia using micro-cantilever bending tests, Mech. Mater. 136 (2019) 103086, https://doi.org/10.1016/j.mechmat.2019.103086.

[19] Y.-H. Ma, Z.-G. Wang, J.-H. Ouyang, S.J. Dillon, L. Feng, Y.-J. Wang, In-situ microcantilever deflection to evaluate the interfacial fracture properties of binary Al₂O₃/SmAlO₃ eutectic, J. Eur. Ceram. Soc. 39 (2019) 3277–3282, https://doi.org/10.1016/j.jeurceramsoc.2019.04.016.

[20] J. Tatami, Y. Imoto, T. Yahagi, T. Takahashi, M. Iijima, Relationship between bending strength of bulk porous silicon carbide ceramics and grain boundary strength measured using microcantilever beam specimens, J. Eur. Ceram. Soc. 40 (2020) 2634–2641, https://doi.org/10.1016/j.jeurceramsoc.2019.12.029.

[21] B.N. Jaya, C. Kirchlechner, G. Dehm, Can microscale fracture tests provide reliable fracture toughness values? A case study in silicon, J. Mater. Res. 30 (2015) 686–698, https://doi.org/10.1557/jmr.2015.2.

[22] B.N. Jaya, J.M. Wheeler, J. Wehrs, J.P. Best, R. Soler, J. Michler, C. Kirchlechner, G. Dehm, Microscale fracture behavior of single crystal silicon beams at elevated temperatures, Nano Lett. 16 (2016) 7597–7603, https://doi.org/10.1021/acs.nanolett.6b03461.

[23] H. Yamaguchi, J. Tatami, T. Yahagi, H. Nakano, M. Iijima, T. Takahashi, T. Kondo, Dislocation-controlled microscopic mechanical phenomena in single crystal silicon under bending stress at room temperature, J. Mater. Sci. 55 (2020) 7359–7372, https://doi.org/10.1007/s10853-020-04528-3.

[24] T. Csanádi, M. Vojtko, Z. Dankházi, M.J. Reece, J. Dusza, Small scale fracture and strength of high-entropy carbide grains during microcantilever bending experiments, J. Eur. Ceram. Soc. 40 (2020) 4774–4782, https://doi.org/10.1016/j.jeurceramsoc.2020.04.023.

[25] T. Csanádi, M. Gall, M. Vojtko, A. Kovalčíková, M. Hnatko, J. Dusza, P. Šajgalík, Microscale fracture strength of grains and grain boundaries in polycrystalline La-doped β-Si₃N₄ ceramics, J. Eur. Ceram. Soc. 40 (2020) 4783–4791, https://doi.org/10.1016/j.jeurceramsoc.2020.04.033.

[26] T. Csanádi, M. Vojtko, J. Dusza, Deformation and fracture of WC grains and grain boundaries in a WC-Co hardmetal during microcantilever bending tests, Int. J. Refract. Met. Hard Mater. 87 (2020) 105163, https://doi.org/10.1016/j.ijrmhm.2019.105163.

[27] M. Tanabe, J. Tatami, M. Iijima, T. Yahagi, T. Takahashi, H. Nakano, T. Ohji, Deformation behaviors and fracture strength of β-Si₃N₄ single crystals, J. Am. Ceram. Soc. 106 (2023) 5431–5439, https://doi.org/10.1111/jace.19167.

[28] Y. Otsuka, J. Tatami, I. Yamamoto, M. Iijima, T. Ohji, Micro- and macro-scale strength properties of c-axis aligned hydroxyapatite ceramics, Ceram. Inter. 49 (2023) 40158–40165, https://doi.org/10.1016/j.ceramint.2023.09.349.

[29] M. Muramoto, J. Tatami, M. Iijima, K. Matsui, T. Yahagi, T. Takahashi, H. Nakano, T. Ohji, Deformation behavior and bending strength of single crystal 8 mol% yttria-stabilized zirconia at microscopic scale, J. Eur. Ceram. Soc. 44 (2024) 1061–1069, https://doi.org/10.1016/j.jeurceramsoc.2023.09.042.

[30] T. Csanádi, A. Azizpour, M. Vojtko, W.G. Fahrenholtz, The effect of crystal anisotropy on fracture toughness and strength of ZrB₂ microcantilevers, J. Am. Ceram. Soc. 107 (2024) 1669–1681, https://doi.org/10.1111/jace.19359.

[31] J. Tatami, M. Uda, T. Takahashi, T. Yahagi, M. Iijima, K. Matsui, T. Ohji, H. Nakano, Microscopic mechanical properties of silicon nitride ceramics corroded in sulfuric acid solution, J. Euro. Ceram. Soc. 44 (2024), https://doi.org/10.1016/j.jeurceramsoc.2023.11.072.

[32] S. Fujita, T. Ohji, T. Yahagi, M. Iijima, J. Tatami, Micro-scale mechanical properties of surface layer in ion-exchanged glass, J. Am. Ceram. Soc. 107 (2024), https://doi.org/10.1111/jace.19755.

[33] T. Csanádi, N.Q. Chinh, P. Szommer, J. Dusza, Z. Lenčés, P. Šajgalík, Deformation and fracture of β-silicon nitride micropillars, J. Am. Ceram. Soc. 98 (2015) 374–377, https://doi.org/10.1111/jace.13402.

[34] A.G. Evans, J.V. Sharp, Microstructural studies on silicon nitride, J. Mater. Sci. 6 (1971) 1292–1302, https://doi.org/10.1007/BF00552043.

[35] X. Milhet, H. Garem, J.L. Demenet, J. Rabier, T. Rouxel, Dislocations studies in β-silicon nitride, J. Mater. Sci. 32 (1997) 3733–3738, https://doi.org/10.1023/A:1018659203552.

[36] H. Suematsu, J.J. Petrovic, T.E. Mitchell, Plastic deformation of silicon nitride single crystals, Mater. Sci. Eng. A. 209 (1996) 97–102, https://doi.org/10.1016/0921-5093(95)10136-5.

[37] J. Weertman, Dislocation Based Fracture Mechanics, World Scientific, Singapore, 1996, https://doi.org/10.1142/3062.

[38] R. Von Mises, Mechanik der plastischen Formaenderung von Kristallen, Z. Angew. Math. Mech. 8 (1928) 161–185, https://doi.org/10.1111/J.1151-2916.1991.TB07132.X.

[39] Y. Huang, J. Jiang, A Critical Review of von Mises Criterion for Compatible Deformation of Polycrystalline Materials, Crystals 13 (2023) 244, https://doi.org/10.3390/cryst13020244.

[40] K. Yasuda, T. Taguchi, J. Tatami, Y. Matsuo, Estimation of short crack R-curves of polycrystalline ceramics by the surface crack in flexure method, Ceram. Trans. 133 (2002) 115–120, https://doi.org/10.1002/9781118371480.ch15.

[41] H. Kleebe, M.K. Chibulk, R.M. Cannon, M. Ruhle, Statistical analysis of the intergranular film thickness in silicon nitride ceramics, J. Am. Ceram. Soc. 76 (1993) 1969–1977, https://doi.org/10.1111/j.1151-2916.1993.tb08319.x.

[42] P.F. Becher, G.S. Painter, M.J. Lance, S. Ii, Y. Ikuhara, Direct observations of debonding of reinforcing grains in silicon nitride ceramics sintered with yttria Plus alumina additives, J. Am. Ceram. Soc. 88 (2005) 1222–1226, https://doi.org/10.1111/j.1551-2916.2005.00237.x.

[43] G.S. Painter, P.F. Becher, W.A. Shelton, R.L. Satet, M.J. Hoffmann, First-principles study of rare-earth effects on grain growth and microstructure in β−Si₃N₄ ceramics, Phys. Rev. B 70 (2004), https://doi.org/10.1103/PhysRevB.70.144108, 144108-1–4.

[44] G.B. Winkelman, C. Dwyer, T.S. Hudson, D. Nguyen-Mahn, M. Doblinger, R. L. Satet, M.J. Hoffmann, D.J.H. Cockayne, Arrangement of rare-earth elements at Prismatic grain boundaries in silicon nitride, Phil. Mag. Lett. 84 (2004) 755–762, https://doi.org/10.1080/09500830500041302.

[45] G.B. Winkelman, C. Dwyer, T.S. Hudson, D. Nguyen-Mahn, M. Doblinger, R. L. Satet, M.J. Hoffmann, D.J.H. Cockayne, Three-dimensional Organization of rare-earth atoms at grain boundaries in silicon nitride, Appl. Phys. Lett. 87 (2005), https://doi.org/10.1063/1.2009067, 061911-1–3.

[46] G.B. Winkelman, C. Dwyer, C. Marsh, T.S. Hudson, D. Nguyen-Mahn, M. Doblinger, D.J.H. Cockayne, The crystal/glass interface in doped Si₃N₄, Mater. Sci. Eng. A 422 (2006) 77–84, https://doi.org/10.1016/j.msea.2006.01.003.

[47] N. Shibata, G.S. Painter, R.L. Satet, M.J. Hoffmann, S.J. Pennycook, P.F. Becher, Rare-earth adsorption at intergranular interfaces in silicon nitride ceramics: Subnanometer observations and theory, Phys. Rev. B 72 (2005), https://doi.org/10.1103/PhysRevB.72.140101, 14101-1–4.

[48] K. van Benthem, G.S. Painter, F.W. Averill, S.J. Pennycook, P.F. Becher, Experimental Probe of Adsorbate binding energies at Internal Crystalline/amorphous interfaces in Gd-doped Si₃N₄, Appl. Phys. Lett. 92 (2008), https://doi.org/10.1063/1.2917566, 16210-1–3.

[49] R.L. Satet, M.J. Hoffmann, Influence of the rare-earth element on the mechanical properties of RE–Mg-Bearing silicon nitride, J. Am. Ceram. Soc. 88 (2005) 2485–2490, https://doi.org/10.1111/j.1551-2916.2005.00421.x.

[50] R.L. Satet, M.J. Hoffmann, R.M. Cannon, Experimental Evidence of the Impact of rare-earth elements on Particle growth and mechanical behavior of silicon nitride, Mater. Sci. Eng. A 422 (2006) 66–76, https://doi.org/10.1016/j.msea.2006.01.015.

[51] H. Gu, R.M. Cannon, I. Tanaka, M. Ruhle, Calcia Partition in phase-Separated intergranular glass and interfaces in doped silicon nitride produced by Hot Isostatic Pressing, Mater. Sci. Eng. A 422 (2006) 51–65, https://doi.org/10.1016/j.msea.2006.01.012.

[52] P.F. Becher, G.S. Painter, N. Shibata, S.B. Waters, H.-T. Lin, Effects of rare-earth (RE) intergranular adsorption on the phase transformation, microstructure evolution, and mechanical properties in silicon nitride with RE2O31MgO additives: RE5La, Gd, and Lu, J. Am. Ceram. Soc. 91 (2008) 2328–2336, https://doi.org/10.1111/j.1551-2916.2008.02448.x.

[53] D.M. Boye, C.P. Ortiz, A.J. Silversmith, N.T.T. Nguyen, K.R. Hoffman, Rare earth ion distribution in sol–gel silicate glasses, J. Lumines. 128 (2008) 888–890, https://doi.org/10.1016/j.jlumin.2007.11.024.

[54] Y. Cheng, H. Xiao, W. Guo, Influence of rare-earth oxides on structure and crystallization properties of Bi_2O_3–B_2O_3 glass, Mater. Sci. Eng. A 480 (2008) 56–61, https://doi.org/10.1016/j.msea.2007.07.071.

[55] R.D. Shannon, C.T. Prewitt, Effective ionic radii in oxides and fluorides, Acta Cryst. B 25 (1969) 925–946, https://doi.org/10.1107/S0567740869003220.

[56] Y. Menke, V. Peltier-Baron, S. Hampshire, Effect of rare-earth cations on properties of sialon glasses, J. Non-Cryst. Solids 276 (2000) 145–150, https://doi.org/10.1016/S0022-3093(00)00268-4.

[57] K. Matsuura, T. Ohji, T. Takahashi, M. Iijima, J. Tatami, Effects of Rare-Earth Oxides on Grain Boundary Strength of Silicon Nitride Ceramics (unpublished work).

[58] E.Y. Sun, P.F. Becher, K.P. Plucknett, C.H. Hsueh, K.B. Alexander, S.B. Waters, K. Hirao, M.E. Brito, Microstructural design of silicon nitride with improved fracture toughness: II, Effects of yttria and alumina additives, J. Am. Ceram. Soc. 81 (1998) 2831–2840, https://doi.org/10.1111/J.1151-2916.1998.TB02703.X.

[59] P.F. Becher, E.Y. Sun, C.-H. Hsueh, K.B. Alexander, S.-L. Hwang, S.B. Waters, C.G. Westmoreland, Debonding of interfaces between beta-silicon nitride whiskers and Si-Al-Y oxynitride glasses, Acta Mater. 44 (1996) 3881–3893, https://doi.org/10.1016/S1359-6454(96)00069-9.

[60] E.Y. Sun, P.F. Becher, C.-H. Hsueh, G.S. Painter, S.B. Waters, S.-L. Hwang, M.J. Hoffmann, Debonding behavior between β-Si_3N_4whiskers and oxynitride glasses with or without an epitaxial β-SiAlON interfacial layer, Acta Mater. 47 (1999) 2777–2785, https://doi.org/10.1016/S1359-6454(99)00122-6.

[61] P.F. Becher, M.J. Lance, M.K. Ferber, M.J. Hoffmann, R.L. Satet, The influence of Mg substitution for Al on the properties of SiMeRE oxynitride glasses, J. Non-Cryst. Solids 333 (2004) 124–128, https://doi.org/10.1016/j.jnoncrysol.2003.09.044.

[62] H. Yamaguchi, T. Nishi, Application of silicon nitride to molten aluminum, Bull. Ceram. Soc. Japan 47 (2012) 32–37.

[63] M.C. Breslin, J. Ringnalda, L. Xu, M. Fuller, J. Seeger, G.S. Daehn, T. Otani, H.L. Fraser, Processing, microstructure, and properties of Co-continuous alumina-aluminum composites, Mater. Sci. Eng. A 195 (1995) 113–119, https://doi.org/10.1016/0921-5093(94)06510-1.

[64] K. Prabriputaloong, M.R. Piggott, Thin-film studies of the reduction of SiO_2 by Al, J. Am. Ceram. Soc. 56 (1973) 177–180, https://doi.org/10.1111/j.1151-2916.1973.tb12449.x.

[65] N. Yoshikawa, A. Kikuchi, S. Tanigucni, Microstructure of Al/Al_2O_3 composite bodies obtained by reaction between $SiO_2$and molten Al at temperatures ranging from 1073 to 1473 K, Mater, Trans. JIM 41 (2000) 399–405, https://doi.org/10.2320/matertrans1989.41.399.

[66] H. Suzuki, T. Ikeda, H. Saito, Preparation and mechanical properties of Y-Si-Al-O-N glass, Bull. Chem. Soc. Japan 5 (1990) 583–588, https://doi.org/10.1246/nikkashi.1990.583.